Research in Astronomy and Astrophysics, 25:085016 (13pp), 2025 August
https://doi.org/10.1088/1674-4527/ade352
CSTR: 32081.14.RAA.ade352

Detecting the Lunar Wrinkle Ridges Through Deep Learning Based on DEM and Aspect Data

Xin Lu[1,2,3], Jiacheng Sun[1,2,3], Gaofeng Shu[1,2,3,4], Jianhui Zhao[1,2,3], and Ning Li[1,2,3]
[1] School of Computer and Information Engineering, Henan University, Kaifeng 475004, China; luxin@henu.edu.cn, gaofeng.shu@henu.edu.cn, hedalining@henu.edu.cn
[2] Henan Province Engineering Research Center of Spatial Information Processing, Kaifeng 475004, China
[3] Henan Key Laboratory of Big Data Analysis and Processing, Kaifeng 475004, China
Received 2025 February 1; revised 2025 May 10; accepted 2025 June 3; published 2025 July 2

Abstract

Lunar wrinkle ridges are an important stress geological structure on the Moon, which reflect the stress state and geological activity on the Moon. They provide important insights into the evolution of the Moon and are key factors influencing future lunar activity, such as the choice of landing sites. However, automatic extraction of lunar wrinkle ridges is a challenging task due to their complex morphology and ambiguous features. Traditional manual extraction methods are time-consuming and labor-intensive. To achieve automated and detailed detection of lunar wrinkle ridges, we have constructed a lunar wrinkle ridge data set, incorporating previously unused aspect data to provide edge information, and proposed a Dual-Branch Ridge Detection Network (DBR-Net) based on deep learning technology. This method employs a dual-branch architecture and an Attention Complementary Feature Fusion module to address the issue of insufficient lunar wrinkle ridge features. Through comparisons with the results of various deep learning approaches, it is demonstrated that the proposed method exhibits superior detection performance. Furthermore, the trained model was applied to lunar mare regions, generating a distribution map of lunar mare wrinkle ridges; a significant linear relationship between the length and area of the lunar wrinkle ridges was obtained through statistical analysis, and six previously unrecorded potential lunar wrinkle ridges were detected. The proposed method upgrades the automated extraction of lunar wrinkle ridges to a pixel-level precision and verifies the effectiveness of DBR-Net in lunar wrinkle ridge detection.

Key words: Moon – methods: data analysis – planets and satellites: surfaces – techniques: image processing

1. Introduction

The lunar geological structure can be broadly classified into linear or circular structures according to the geometric characteristics (Lu et al. 2022). A lunar wrinkle ridge is one of the most common linear structures on the lunar surface. It is a mountain ridge formed by the extrusion of stress inside the Moon (Schultz 2000), which is related to the stress state inside the Moon. Studying the lunar wrinkle ridges is helpful for understanding the stress field and evolution history of the Moon.

In previous studies, the methods for detecting lunar wrinkle ridges could be classified into manual visual interpretation methods and automated methods. Yue et al. (2015) used optical data and manual visual methods to extract lunar wrinkle ridges. Yao & Chen (2018) visually identified the lunar wrinkle ridges on the Digital Elevation Model (DEM) data. These studies were pioneering in determining the direction and distribution of lunar wrinkle ridges. However, the manual extraction method is inefficient and labor-intensive, limiting its applicability for large-scale identification of lunar wrinkle ridges. To address these limitations, automated extraction methods based on traditional image processing techniques have been developed. Lou & Kang (2018) utilized the specificity of the lunar linear structure in elevation and applied multiple average filtering on the DEM data to extract the linear structure. Micheal et al. (2014) calculated the phase symmetry of slope information and extracted the lunar wrinkle ridges based on DEM data. Jiang et al. (2015) employed a block clustering algorithm based on image features for terrain classification of Chang'e-1 Charge Coupled Device (CCD) Stereo Camera images. These traditional image processing methods enhance extraction efficiency and are straightforward to implement. Nevertheless, they primarily identify ridge lines that indicate the general trend, failing to capture the complete shape or edges of the lunar wrinkle ridges. Additionally, the effectiveness of the method is highly dependent on the selection of an appropriate threshold.

The general orientation of lunar wrinkle ridges can indeed be determined; however, considerable potential exists for enhanced precision in their identification. From a morphological perspective, lunar wrinkle ridges exhibit a complex and varied topography, complicating the accurate delineation of

[4] Corresponding author.

their boundaries and fine details based solely on elevation data. Moreover, conventional image processing techniques are substantially threshold-dependent, which impedes their efficacy in identifying the intricately undulating features characteristic of the lunar wrinkle ridges. Consequently, it is imperative to address and mitigate these limitations to improve the accuracy and reliability of lunar wrinkle ridge identification. This requires the development and application of advanced methods that can effectively capture the nuanced topography and reduce the threshold dependency inherent in traditional approaches.

In the field of planetary image processing in astronomy, many researchers have successfully applied deep learning methods to achieve excellent results, enabling more precise image segmentation and image classification. For instance, Silburt et al. (2019) applied U-Net to automatically detect craters, while Zhang et al. (2024) utilized an improved Deeplabv3+ model to identify lunar sinuous rilles. Peng et al. (2023) utilized deep learning methods based on Convolutional Neural Networks (CNNs) and transformers to achieve fine structure segmentation of magnetic bright point images. Li et al. (2024) integrated CNNs and Support Vector Machines (SVMs) to identify contaminated images in light curve data preprocessing. These studies collectively underscore the substantial potential of deep learning in the realm of astronomical image processing, highlighting its capability to enhance the accuracy and efficiency of data analysis in this field.

Inspired by the widespread application of deep learning techniques in astronomical image processing, this study aims to tackle the challenges of insufficient detail and low efficiency in recognizing lunar wrinkle ridges. To achieve this, we have constructed a deep learning data set for lunar wrinkle ridge detection through manual annotation. This data set encompasses DEM data, aspect data, and corresponding label data. Notably, the aspect data have been identified as a significant feature for delineating ridge edges. In light of this, we propose a Dual-Branch Ridge Detection Network (DBR-Net) to address the complexities of lunar wrinkle ridge morphology and edge detection.

The DBR-Net architecture consists of a dual-branch encoder that separately extracts body features from the DEM data and edge features from the aspect data representation. To effectively fuse these multi-source features, an Attention Complementary Feature Fusion (ACFF) module is well-designed and incorporated. This module ensures that the integration of body and edge features is both robust and complementary, enabling the network to accurately delineate both the shape and edges of the lunar wrinkle ridges.

The proposed DBR-Net achieves a significant improvement in the resolution of ridge extraction, refining the representation from coarse ridge lines to precise pixel-level edge delineation. Experimental results validate the efficacy of the proposed method, demonstrating its superior performance in lunar wrinkle ridge detection. As a direct outcome of this research, a detailed map of the distribution of wrinkle ridges within the lunar mare has been generated, and six previously unrecorded lunar wrinkle ridges being identified, highlighting the potential for new scientific discoveries in lunar morphology.

2. Data

The development of a high-quality and accurate data set for lunar wrinkle ridge detection is a critical prerequisite for training and validating deep learning models in this domain. Previous works have been constrained by the limited availability of such data sets, impeding progress in this field. To address this issue, this study constructs a comprehensive deep learning data set specifically designed for lunar wrinkle ridge detection. The data set integrates DEM data and aspect data, both of which are essential for capturing the topographic and morphological characteristics of lunar wrinkle ridges. This data set serves as a foundational resource for model training, evaluation, and benchmarking, thereby facilitating more accurate and reliable detection of lunar wrinkle ridges in future research.

2.1. Study Area

Lunar wrinkle ridges are predominantly found in the lunar mare regions. Therefore, the study area for this research is specifically selected within the lunar mare. The data set was created using data from a region spanning longitudes 90°W–45°W and latitudes 0–60°N. This region was chosen for its rich distribution of lunar wrinkle ridges and the availability of DEM and aspect data. The trained model was subsequently applied to detect lunar wrinkle ridges in a broader area, covering longitudes 90°W–45°E and latitudes 30°S–60°N, encompassing nearly the entire lunar mare. This extended coverage allows for a comprehensive evaluation of the model's performance and the identification of potential unrecorded lunar wrinkle ridges within the lunar mare. The study area is illustrated in Figure 1.

2.2. Data Type

The field of lunar terrain recognition primarily relies on two types of data: optical imagery and DEM data. While optical imagery offers the advantage of high resolution, the accurate identification of lunar wrinkle ridges is often hindered by variations in illumination conditions. Qiao et al. (2021) stated that different illumination conditions have a significant impact on the accurate recognition of lunar terrain in optical imagery, leading to potential inaccuracies in feature extraction. In contrast, DEM data are inherently independent of illumination conditions and provide rich structural feature information,

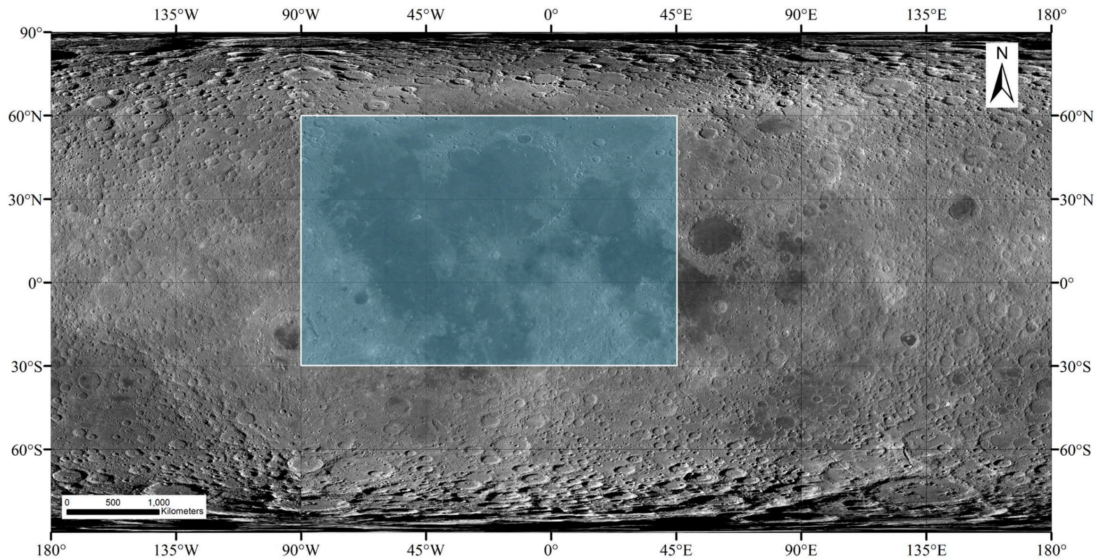

Figure 1. Study Area.

making them a more robust resource for morphological feature analysis. DEM data not only circumvent the limitations imposed by illumination variations but also capture critical topographic details, such as elevation profiles and ridge geometries, which are essential for the precise identification of lunar wrinkle ridges. Given these advantages, this study employs DEM data acquired from the Lunar Orbiter Laser Altimeter (LOLA) instrument onboard the Lunar Reconnaissance Orbiter for lunar wrinkle ridge identification.

However, in terms of representing lunar wrinkle ridges, both optical imagery and DEM data have limitations, specifically manifested in inadequate representation of edge features. The typical feature of lunar wrinkle ridges is their gentle-to-steep slope, which results in a blurry boundary between lunar wrinkle ridges and surrounding landforms, significantly increasing the complexity of identification. Both optical data and DEM data face notable difficulties in distinguishing the edges of lunar wrinkle ridges from the surrounding landforms, leading to previous studies being able to identify only the ridge lines of lunar wrinkle ridges but not achieving an accurate depiction of their overall structure. Therefore, exploring and developing new types of data with edge representation capabilities are of crucial importance for achieving accurate recognition of lunar wrinkle ridges.

To capture the edges of the lunar wrinkle ridges, we introduced aspect data. Slope is the first derivative of a surface and has both magnitude and direction. Aspect is the bearing (or azimuth) of the slope direction. Aspect is defined as the compass direction of steepest downhill slope, with an angular range from 0° to 360°. The aspect data identify the downslope direction of the maximum rate of change in value from each pixel to its neighboring pixels. In the aspect data, the downslope at the edges of the lunar wrinkle ridges exhibits similar values. Therefore, the aspect data are sensitive to the ridge edges, which complement the main body features of the ridges represented by DEM data.

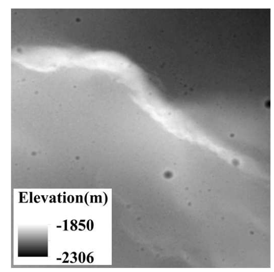

Figure 2. DEM data.

Given these advantages, this study employs DEM data and aspect data for lunar wrinkle ridge identification.

2.3. Data Source and Processing

The DEM data we used were those presented by Barker et al. (2016), in which the DEM co-registered the Terrain Camera data with LOLA instrument geodetic accuracy data called SLDEM2015. Figure 2 shows the DEM data. The horizontal resolution of these DEM data is 512 pixels/degree (59 m/pixel) and a typical vertical accuracy is 3–4 m. These data are archived in the Planetary Data System (PDS) and can be accessed via https://pds-geosciences.wustl.edu/lro/lro-l-lola-3-rdr-v1/lrolol_1xxx/data/sldem2015/tiles/float_img.

The aspect data are created from the DEM data by the Geospatial Data Abstraction Library (GDAL). GDAL is a translator library for raster and vector geospatial data formats.

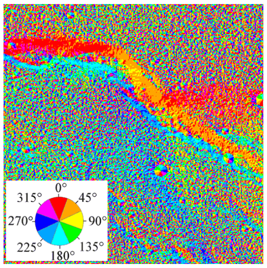

Figure 3. Aspect data.

We utilize its Python version to derive aspect data from DEM data by invoking the `gdal.DEMProcessing` command. The calculation process for aspect data (Burrough et al. 2011) is as follows. Suppose the surface function is

$$z = f(x, y), \tag{1}$$

where z is altitude and x and y are the coordinate axes.

Then, the slope is defined as

$$\text{Slope}_x = \frac{df}{dx} = f_x, \tag{2}$$

$$\text{Slope}_y = \frac{df}{dy} = f_y, \tag{3}$$

such that Slope_x and Slope_y are the slopes in the row (x) and column (y) directions respectively.

The aspect is given by

$$\text{Aspect} = \arctan\left(\frac{\text{Slope}_y}{\text{Slope}_x}\right). \tag{4}$$

The aspect values represent the compass direction values (0°–360°). Figure 3 shows the aspect data.

In digital terrain modeling, aspect data can be derived from the DEM data using simple local operations. The aspect value of each pixel is usually calculated from the data in a continuously moving 3 × 3 sliding window on the map. The sliding window used in the calculation is illustrated in Figure 4. The slopes of pixel e_5 in the row (x) and column (y) directions can be expressed as:

$$\text{Slope}_x = \frac{(e_3 + 2e_6 + e_9) - (e_1 + 2e_4 + e_7)}{8}. \tag{5}$$

$$\text{Slope}_y = \frac{(e_7 + 2e_8 + e_9) - (e_1 + 2e_2 + e_3)}{8}. \tag{6}$$

The aspect value of pixel e_5 can be obtained from Equation (4).

In addition, variance filtering is used to process the aspect data. This technique utilizes a sliding window, as illustrated in Figure 4, and the calculation formula for variance filtering is shown as follows.

$$S(e_5) = \frac{\sum_{i=1}^{9}(e_i - \bar{e})^2}{9}, \tag{7}$$

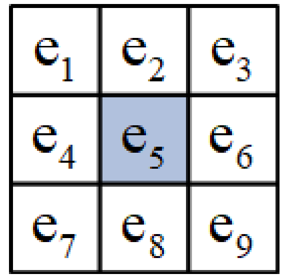

Figure 4. Sliding window.

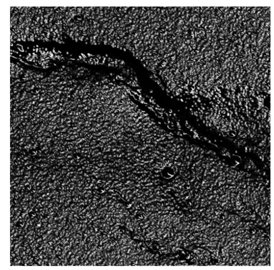

Figure 5. Aspect data after variance filtering.

where $\bar{e}$ represents the average value of the sliding window. $S(e_5)$ is the pixel value in the aspect image after variance filtering. This process results in consistently lower values for the downhill areas of lunar wrinkle ridges, and highlights slopes in similar directions, differentiating them from the surrounding terrain. Therefore, the edge characterization ability of aspect data is enhanced. The aspect data after variance filtering are depicted in Figure 5.

2.4. Data Set

The data set is constructed by manually labeling the lunar wrinkle ridges based on the DEM data and aspect data after applying variance filtering. In the process of manual labeling, Yue et al. (2015) provide some of the explored lunar wrinkle ridge position coordinates. In order to facilitate deep learning applications, the sliding window clipping method is used to cut the image into 1069 blocks, each measuring 512 × 512 pixels. These blocks are then partitioned into training and testing sets with a ratio of 8:2.

3. Method

3.1. Overview

A dual-branch lunar wrinkle ridge detection network was utilized to detect lunar wrinkle ridges, as illustrated in Figure 6. The model integrates semantic segmentation, an attention mechanism, and feature-level fusion (Feng et al. 2020). Building on the excellent performance of DeepLabV3+ (Chen et al. 2018) in the field of remote sensing and the effectiveness of the Atrous Spatial Pyramid Pooling (ASPP) module (Chen et al. 2017) for

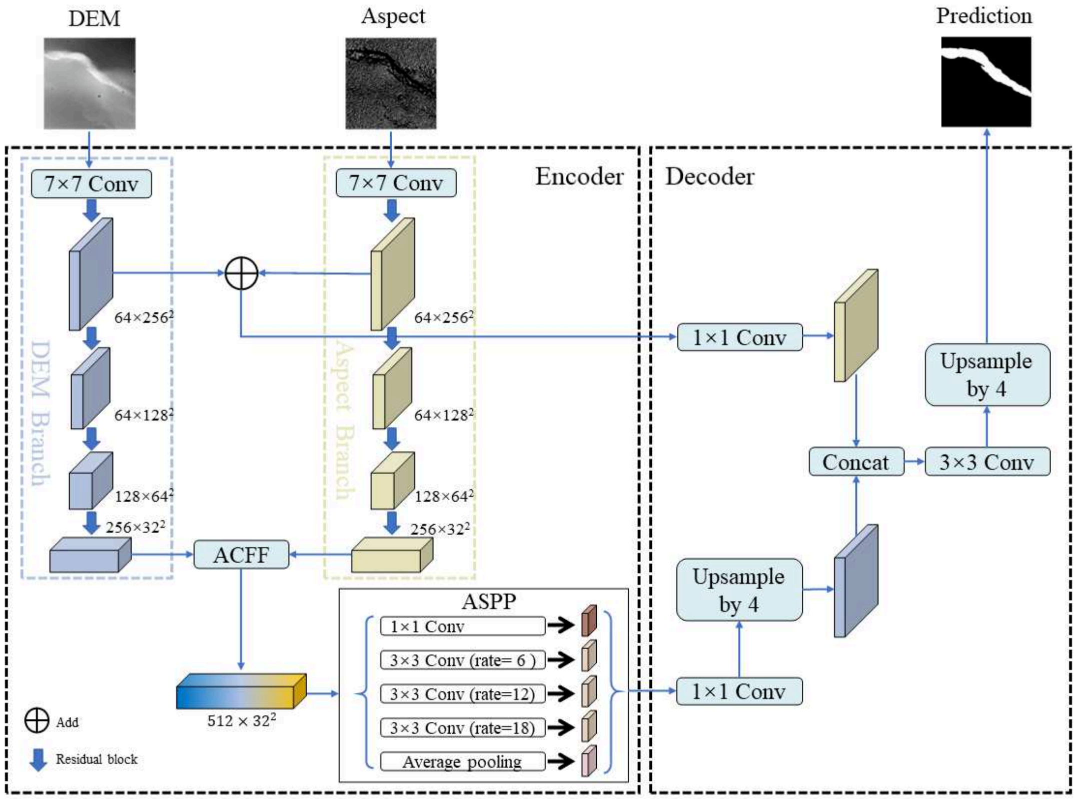

Figure 6. Structure of DBR-Net.

multi-scale target detection, we developed DBR-Net as an improvement upon DeepLabV3+. The network takes DEM data and aspect data as input, with a dual-branch feature encoder that extracts multi-level features independently. The semantic information from the dual-branch high-level features is fused using the ACFF module. The rich spatial detail from the low-level features is merged with the high-level features through skip connections. Finally, the decoder transforms the combined feature map into segmentation results.

3.1.1. Dual-branch Feature Encoder

The dual-branch feature encoder consists of residual blocks and initially utilizes a dual-branch architecture to extract features independently. It then fuses both branches to enhance feature representations. Two Resnet-34 models, pre-trained on the ImageNet data set, serve as the backbone network for feature extraction. The structure of both branches is identical. ResNet-34 incorporates residual modules designed to facilitate efficient learning and address the vanishing gradient problem. Moreover, compared with the ResNet-18 and ResNet-50 variants, ResNet-34 achieves the best balance between network performance and computing efficiency. This architecture provides sufficient feature representation capacity to effectively capture contextual information, while simultaneously maintaining reduced computational and memory requirements. As proposed in ResNet (He et al. 2016), we set 3, 4, 6, 3 residual blocks at each stage. Upon receiving the DEM and aspect data, the dual-branch encoder extracts features separately. This process results in two distinct types of features, each containing multiple levels. The dual-branch encoder structure effectively captures the body features of lunar wrinkle ridges from the DEM data and the edge features from the aspect data.

A large number of studies have tried to fuse different feature information, enhancing the informational richness of the fusion results and significantly advancing research in complex visual tasks (Ebel et al. 2020; Ye et al. 2024). The multi-type and multi-level features extracted by the dual-branch encoder structure provide a foundation for more flexible feature fusion methods (Feng et al. 2020). Low-level features contain rich spatial information, while high-level features contain semantic information. Based on these characteristics, this study developed distinct feature fusion methods. For low-level features, an additive approach is used to augment the information available in the spatial dimension. For high-level features, an ACFF module based on the attention mechanism is designed.

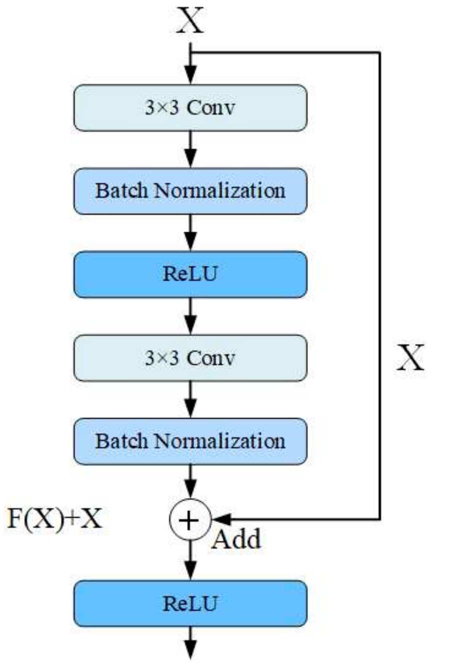

Figure 7. Residual block structure.

3.1.2. Backbone of Dual-branch Feature Encoder

In order to fully extract and integrate two different features, the encoder module is designed with a dual-branch architecture. Each branch employs ResNet-34 as the backbone. ResNet-34 incorporates residual modules designed to facilitate efficient learning and address the vanishing gradient problem. Moreover, there is a relatively shallow architecture in ResNet-34 that effectively captures contextual information while reducing computational and memory demands.

To tackle the training challenges of deep networks, ResNet introduced a pivotal innovation: the residual block. The architecture of ResNet was introduced by He et al. (2016). The structure of a residual block is illustrated in Figure 7. The core idea of a residual block is to introduce a Residual Connection, which permits the input to be directly passed to subsequent layers and summed with the output after convolutional operations. The residual block adds a shortcut connection before the second ReLU activation function, transforming the input of the activation function from the original $H(X) = F(X)$ to $H(X) = F(X) + X$. This design enables residual blocks to learn identity mapping more easily, thereby avoiding information loss in deep networks. As a result, it achieved significant success in image classification and computer vision tasks.

In this study, we imported modules such as `Resnet` and `BasicBlock` from `torchvision.model.resnet` and used these modules to construct ResNet-34. The architecture of the encoder is reconstructed and the dual-branch feature encoder is constructed.

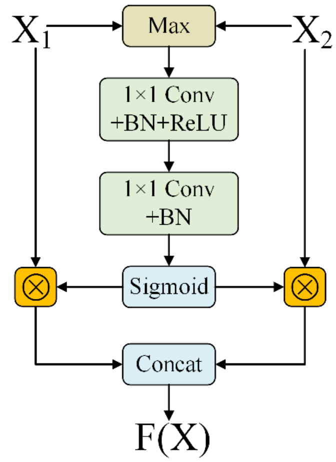

Figure 8. ACFF module structure.

3.1.3. Attention Complementary Feature Fusion Module

ACFF module, which is based on an attention mechanism, is designed to effectively fuse high-level semantic information, thereby enhancing the model's ability to distinguish between lunar wrinkle ridges and backgrounds. The structure of the ACFF module is shown in Figure 8. First, a maximization method is applied to the feature maps from the DEM branch and the aspect branch to combine the most significant features from both maps. Point-wise convolution serves as the local channel context aggregator, exploiting point-wise channel interactions for each spatial position. The significant features obtained after maximization emphasize the entire lunar wrinkle ridge structure through feature mapping via point-wise convolution and channel attention, which is based on local spatial information. The local channel context $L(X) \in \mathbb{R}^{C\times H\times W}$ can be calculated as follows

$$L(X) = \beta(\mathrm{Conv}_2(\gamma(\beta(\mathrm{Conv}_1(\mathrm{Max}(X_1, X_2)))))). \tag{8}$$

Here, γ denotes the ReLU activation function, β denotes batch normalization, Max denotes maximization calculation, and Conv is the 1×1 convolution blocks. Finally, we can calculate the fused features $F(X) \in \mathbb{R}^{C\times H\times W}$ using the provided local channel context $L(X)$.

$$F(X) = \mathrm{Concat}(X_1 \otimes \sigma(L(X)), X_2 \otimes \sigma(L(X))). \tag{9}$$

Here, Concat denotes the concatenation operation. $\otimes$ denotes elementwise multiplication. σ denotes the sigmoid function. The elementwise multiplication operation is used to weight the input feature map. At deeper levels of the model, an increased number of features enables the model to more effectively capture the relationships among different features. Therefore, we apply the concatenation operation in conjunction with the weighted features to enhance the diversity of feature types.

Table 1
Hyperparameter Settings

Configuration	DBR-Net
Optimizer	SGD
Batch size	4
Total-train-epoch	60
Initial learning rate	1×10^{-3}
Period of learning rate decay	20 epochs
Multiplicative factor of learning rate decay	0.1
Loss function	Binary Cross-Entropy Loss
Operating system	MS Windows 10
Graphics processing unit (GPU)	NVIDIA RTX A5000 24 GB
Programming language	Python 3.12
Development environment configuration	Pytorch 2.2 and CUDA 11.7

4. Experiments and Results

4.1. Implementation Details

All experiments are conducted using the PyTorch deep learning framework. The binary cross-entropy loss function is employed, with the stochastic gradient descent (SGD) algorithm serving as the optimizer. The initial learning rate is set to 1×10^{-3}, and a learning rate decay strategy is adopted, reducing the rate to 0.1 times the original value every 20 epochs. The entire training cycle contains 60 epochs. All experiments were performed on a computer equipped with an NVIDIA RTX A5000 GPU and an Intel Xeon Gold 6126 CPU. Table 1 presents the hyperparameter settings for DBR-Net and the hardware environment used in this experiment.

4.2. Evaluation Metrics

To comprehensively assess the performance of the proposed model, we employed the confusion matrix as the primary evaluation tool. The confusion matrix, a specific type of tabular layout, visually represents the correspondence between the model's predictions and the actual classes, particularly suitable for binary classification tasks. In this study, the binary classification task involved categorizing images into "Class A" (lunar wrinkle ridges class) and "Class B" (background class).

The specific form of the confusion matrix is shown in Table 2.

True Positives (TP) represent the number of samples correctly predicted as Class A. False Negatives (FN) represent the number of samples incorrectly predicted as Class B but actually belonging to Class A. False Positives (FP) represent the number of samples incorrectly predicted as Class A but actually belonging to Class B. True Negatives (TN) represent the number of samples correctly predicted as Class B.

By analyzing the confusion matrix, the commonly utilized evaluation metrics of semantic segmentation (precision, recall, F1-score and IoU) are utilized as the objective evaluation

Table 2
Confusion Matrix

	Predicted as Class A	Predicted as Class B
Actual Class A	TP (True Positives)	FN (False Negatives)
Actual Class B	FP (False Positives)	TN (True Negatives)

metrics of this study to evaluate the lunar wrinkle ridge detection ability of the network. Their calculation formula is as follows

$$\text{Precision} = \frac{\text{TP}}{\text{TP} + \text{FP}}. \tag{10}$$

Precision is the proportion of actual "lunar wrinkle ridges class" samples among all samples predicted as "lunar wrinkle ridges class," and it reflects the model's accuracy in predicting the positive class ("lunar wrinkle ridges class").

$$\text{Recall} = \frac{\text{TP}}{\text{TP} + \text{FN}}. \tag{11}$$

Recall is the proportion of actual "lunar wrinkle ridges class" samples correctly predicted as "lunar wrinkle ridges class," and it measures the model's ability to identify positive class samples.

$$\text{F1} = \frac{2 \times \text{precision} \times \text{recall}}{\text{precision} + \text{recall}}. \tag{12}$$

F1-score is the harmonic mean of precision and recall, and it is a comprehensive metric that balances the importance of precision and recall.

$$\text{IoU} = \frac{\text{TP}}{\text{TP} + \text{FP} + \text{FN}}. \tag{13}$$

IoU represents intersection over union of the model predictions to the true values, which is commonly used to measure the segmentation effectiveness of the model.

In the experiments and results section, we comprehensively evaluate our experimental results using the aforementioned metrics.

4.3. Comparison Experiments

In this section, we aim to verify the performance of the proposed model and evaluate the contribution of aspect data to the detection results. Since our method yields pixel-level extraction results of lunar wrinkle ridges, which cannot be compared with traditional image processing methods that only extract ridge lines, we have chosen several mainstream deep learning-based semantic segmentation methods for comparison. The performance comparison of different data is to explore the contribution of aspect data to the detection results, and the performance comparison of different methods is to verify the performance of the proposed methods. DBR-Net is

Table 3
Performance Comparison of Different Data and Methods

Method	Data	Precision (%)	Recall (%)	F1 (%)	IoU (%)
FCN	DEM	85.06	71.54	77.71	63.55
	DEM+Aspect	86.07	73.74	79.43	65.88
RefineNet	DEM	83.77	74.96	79.12	65.45
	DEM+Aspect	84.93	75.25	79.79	66.38
PSPNet	DEM	84.29	72.99	78.23	64.25
	DEM+Aspect	87.01	72.87	79.31	65.82
DeepLabV3+	DEM	86.18	73.78	79.50	66.01
	DEM+Aspect	88.70	74.15	80.75	67.72
Ours	DEM+Aspect	**89.20**	**78.42**	**83.46**	**71.61**

The bold values are defined as the best performance metrics.

compared with other mainstream semantic segmentation models, including FCN, RefineNet, PSPNet, and DeepLabV3+. The models used separate DEM data as well as combined DEM and aspect data. The model was trained and tested using the manually annotated lunar wrinkle ridge data set from this study. To ensure fairness in the experiments, all experiments were conducted under the same environmental and hardware conditions. The corresponding performance indicators are presented in Table 3.

4.3.1. Performance Comparison of Different Data

To assess the effectiveness of incorporating aspect data, we utilized both only DEM data set and a combination of DEM and aspect data as inputs for the model. In this study, four comparison methods use a concatenation method to merge these two types of data, creating dual-channel data for single-branch input. The proposed model, on the other hand, processes both data types through a dual-branch architecture. The results indicate that the comprehensive evaluation metrics (F1-score and IoU) for the detection outcomes of all models improved when using the combined DEM and aspect data, as opposed to using DEM data alone. This enhancement is primarily attributed to the aspect data's provision of the ridge edge features that are absent in the DEM data. Compared to using only DEM data, the combined use of DEM data and aspect data demonstrates significant advantages. On the one hand, the edges of lunar wrinkle ridges and the surrounding terrains do not exhibit large differences in elevation, rendering the elevation features relatively inconspicuous. DEM data can effectively represent ridges with significant elevation differences but lack the ability to characterize the edges of lunar wrinkle ridges. On the other hand, aspect data leverage the information of continuous change rates in terrain and can represent the gradually changing edges of lunar wrinkle ridges. Compared to DEM data, aspect data can capture more terrain information. By combining these two types of data, integrating the body features and edge features of lunar wrinkle ridges can provide more valuable spatial information for lunar wrinkle ridge extraction.

4.3.2. Performance Comparison with Different Methods

Compared to lunar wrinkle ridge automation extraction methods based on traditional image processing techniques, deep learning methods enhance the extraction results from a coarse representation of ridge lines to a pixel-level representation of lunar wrinkle ridge edges. Figure 9 qualitatively shows the results of lunar wrinkle ridge extraction by applying different deep learning methods across multiple scenarios, using combined DEM data and aspect data. While all methods successfully capture the primary structure and orientation of the lunar wrinkle ridges, DBR-Net demonstrates superior effectiveness in detailing the intricacies and edges of the ridges, preserving smaller lunar wrinkle ridges and providing more accurate ridge contours. Compared to other models, the proposed model achieves the highest precision (89.20%), recall (78.42%), F1-score (83.46%), and IoU (71.61%). When compared to the original DeepLabV3+, the DBR-Net shows an increase in precision by 0.5%, recall by 4.27%, F1-score by 2.71%, and an increase in IoU by 3.89%. These improvements can be attributed to the dual-branch structure and the ACFF module. These components enhance the model's flexibility in addressing complementary features and enable more effective fusion of these features through the attention mechanism. As a result, they help the model gain a better understanding of the data and improve overall performance.

4.4. Ablation Study

We performed relevant ablation studies to verify the function of the component modules in our proposed DBR-Net, as shown in Table 4. The baseline model refers to the unmodified DeeplabV3+. Compared with single-branch models, dual-branch models utilizing Add/Concat feature fusion methods demonstrate partial improvement by simultaneously processing both body and edge features of lunar wrinkle ridges, yet fail to effectively integrate their differentiated characteristics. The ACFF module effectively integrates the two types of features, enhancing the capture of contours of the lunar wrinkle ridges and significantly improving recall and overall metrics. The experimental results demonstrate the necessity of using both the dual-branch structure and the ACFF module together.

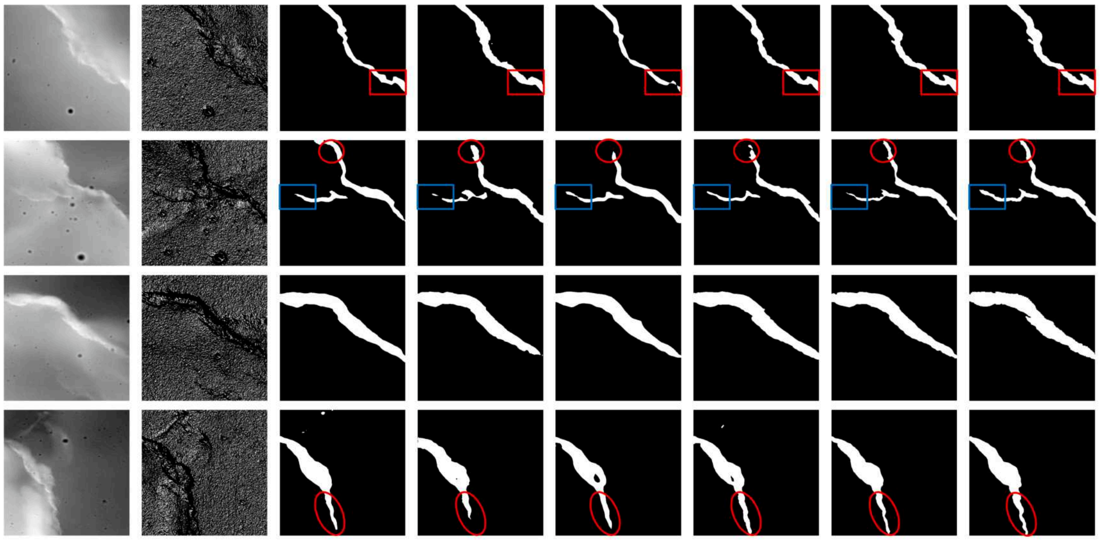

Figure 9. Performance comparison with different methods.

Table 4
Results of Ablation Studies

Method	Components			Precision (%)	Recall (%)	F1 (%)	IoU (%)
	Baseline	Dual-Branch	Feature Fusion Method				
Method1	✓	×	×	88.70	74.15	80.75	67.72
Method2	✓	✓	Add	88.62	75.23	81.37	68.93
Method3	✓	✓	Concat	88.78	75.85	81.76	69.15
DBR-Net	✓	✓	ACFF	**89.20**	**78.42**	**83.46**	**71.61**

4.5. Transfer Learning Experiment

Mars also exhibits wrinkle ridges similar to those found on the Moon. Although Mars and the Moon differ in environmental and geological contexts, the wrinkle ridges on these planetary bodies share fundamental morphological characteristics, such as linear structures and central elevated crests. This similarity provides a basis for the transferability of models, motivating the use of manually labeled Martian wrinkle ridges to evaluate the generalization capability of DBR-Net.

The Martian DEM data used in this study were sourced from the Mars HRSC MOLA Blended DEM Global 200 m v2 (Fergason et al. 2018), which combines DEM data from the Mars Orbiter Laser Altimeter (MOLA) and the High-Resolution Stereo Camera (HRSC) with a resolution of 200 m pixel^{-1}. The images were normalized to reduce domain shift, and wrinkle ridges at multiple sites on Mars were manually annotated to serve as a validation data set. The images were then cropped to 512×512 pixels to meet the model's input requirements, with a total of 110 Martian wrinkle ridge images used for testing. A small subset of regions was selected to visualize DBR-Net's prediction results, as shown in Figure 10. By comparing the predicted Martian wrinkle ridges with the ground truth labels, the quantitative evaluation metrics for the test images obtained by DBR-Net were IoU = 62.3% and F1 = 77.1%. This transfer experiment demonstrates that, despite interplanetary geological differences, certain features remain transferable, confirming DBR-Net's generalization ability and its capacity to learn ridge morphology across planetary bodies.

5. Discussion

The trained DBR-Net was applied to detect ridges in the lunar mare within a latitude range of 30°S to 60°N and a longitude range of 90°W–45°E. For optimal visualization clarity and resolution, the results presented in the main text focus on a representative sector spanning 30°N–60°N latitude and 90°W–0°

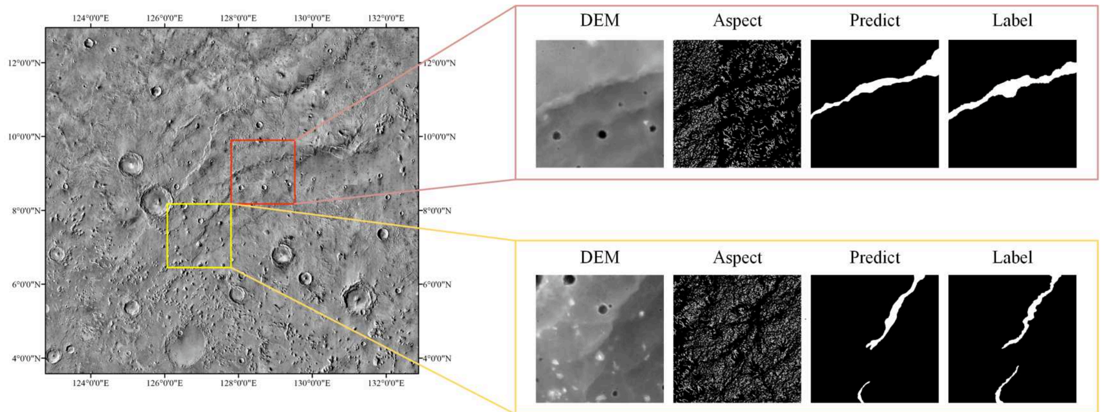

Figure 10. Results of Martian wrinkle ridge detection. (The base map utilizes Thermal Emission Imaging System (THEMIS) infrared data from Mars Odyssey.)

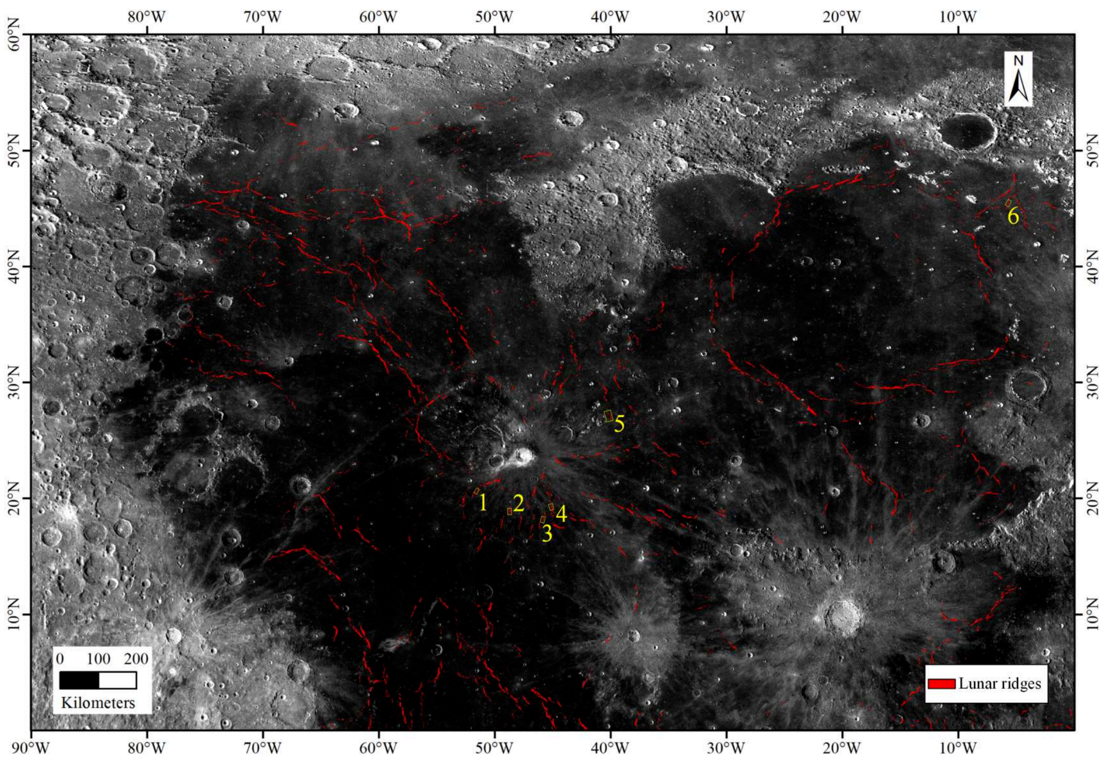

Figure 11. The lunar wrinkle ridge distribution map of the lunar mare. The base image is a WAC optical image.

longitude, as shown in Figure 11. The complete large-scale extraction results are provided as supplementary materials, accessible at https://zenodo.org/records/15365723.

This map delineates the outlines of lunar wrinkle ridge edges, serving as a supplement to the existing ridge line maps of lunar wrinkle ridges from previous studies. It provides information on the length, width, and area of lunar wrinkle ridges, a significant linear relationship between the length and area of the lunar crease ridges is obtained. Furthermore, through a comparative analysis with a manually labeled data set and existing lunar wrinkle ridge catalogs, six previously unrecorded potential lunar wrinkle ridges were detected. Morphological analysis and three-dimensional (3D) visualization representations were conducted on these potential lunar wrinkle ridges to validate and demonstrate the effectiveness of the proposed method.

5.1. Lunar Wrinkle Ridge Detection

Based on the manually labeled lunar wrinkle ridges provided by Yue et al. (2015), we developed a lunar wrinkle

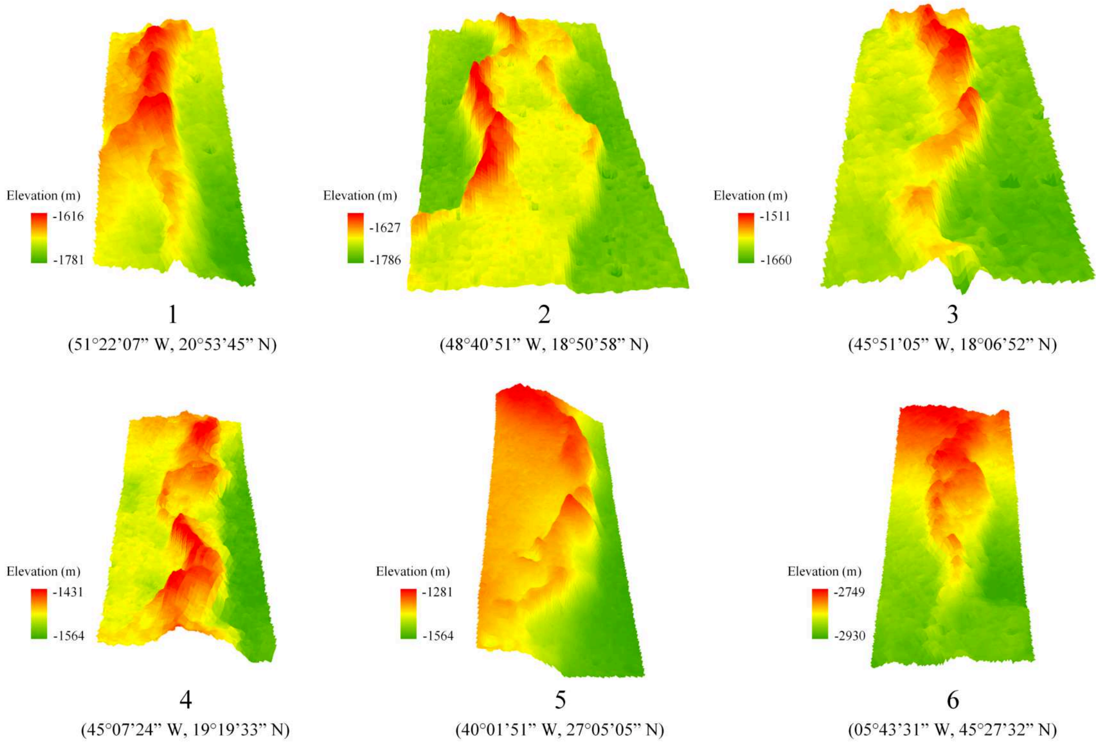

Figure 12. 3D reconstruction results of newly detected potential lunar wrinkle ridges.

ridge data set. Using the trained DBR-Net, we inferred on each image to obtain a more refined extraction of lunar wrinkle ridges. Figure 11 displays the morphological delineation and distribution of wrinkle ridges in the lunar mare regions identified in this study. The red pixels represent the lunar wrinkle ridges detected by our model, while the yellow numbers identify newly detected potential lunar wrinkle ridges. We speculate that these newly detected potential lunar wrinkle ridges may have degraded over time due to their advanced age, resulting in similar textural features to the surrounding terrain in optical images, which makes them difficult to identify through conventional manual visual interpretation. In this study, by utilizing DEM data and aspect data, we successfully detected these potential lunar wrinkle ridges based on terrain variation information.

5.2. Morphological Analysis of Potential Lunar Wrinkle Ridges

Table 5 provides the latitude and longitude coordinates, length, width, and height of six newly detected potential lunar wrinkle ridges. When compared with established lunar wrinkle ridges, the morphological parameters of these newly detected features fall within a reasonable range. Furthermore, we reconstructed 3D models of these potential lunar wrinkle ridges using DEM data and the 3D visualizations are presented in Figure 12. From this figure, it is evident that the potential lunar wrinkle ridges exhibit morphological characteristics similar to those of established lunar wrinkle ridges. The experimental results demonstrate the effectiveness of deep learning techniques in the identification of lunar wrinkle ridges. These findings not only validate the performance of the DBR-Net model but also highlight the significant potential of deep learning in other terrain recognition domains.

Table 5
Newly Discovered Potential Lunar Wrinkle Ridges and Their Characteristics

Number	Longitude	Latitude	Length (m)	Width (m)	Height (m)
1	51°22′07″ W	20°53′45″ N	8264	974	151
2	48°40′51″ W	18°50′58″ N	14496	1271	355
3	45°51′05″ W	18°06′52″ N	8887	772	149
4	45°07′24″ W	19°19′33″ N	11521	1524	133
5	40°01′51″ W	27°05′05″ N	26764	2461	223
6	05°43′31″ W	45°27′32″ N	11734	2663	181

5.3. Statistical Analysis of Lunar Wrinkle Ridges

Based on pixel-level identification, we conducted a systematic parametric statistical analysis of over 3000 lunar wrinkle ridge segments across the entire lunar mare, revealing

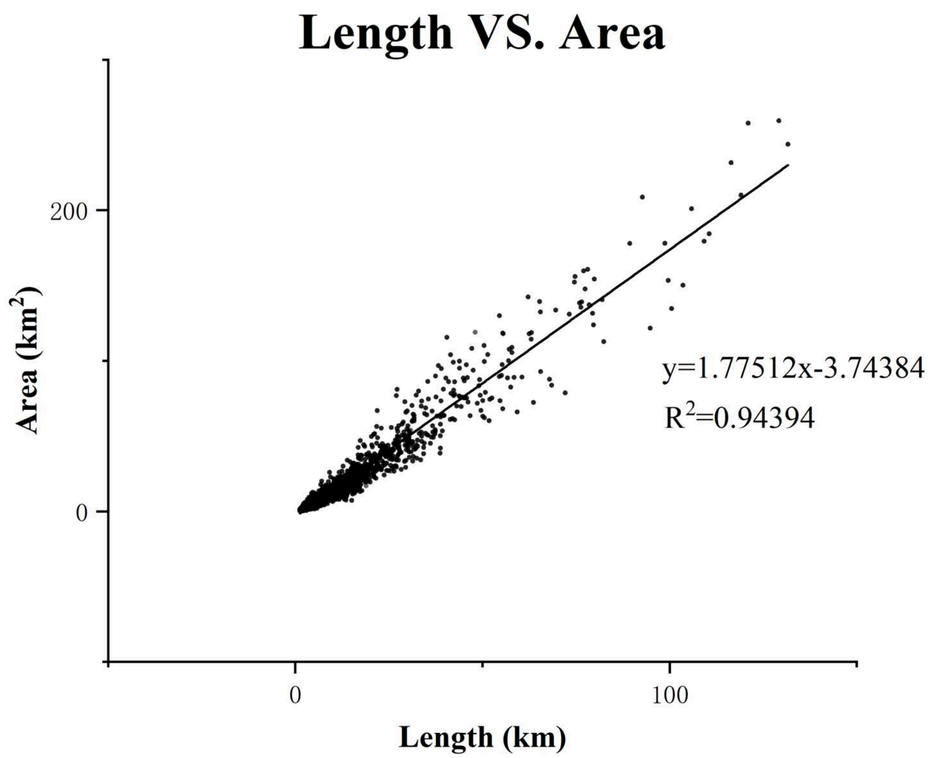

Figure 13. Length-to-area relationship.

a significant linear relationship between ridge length and area, as illustrated in Figure 13.

The establishment of this quantitative relationship provides a new scaling reference for studies of lunar tectonic evolution. The linear correlation between length and area sheds new light on wrinkle ridge formation mechanisms, suggesting their development under a unified lunar stress field. This finding supports dynamic models capable of explaining ridge formation processes and aligns with conclusions by Yue et al. (2015) that lunar wrinkle ridges form mainly through tectonic activity, not solely from volcanic origins or pre-mare buried structures. Previous studies on the formation mechanism of lunar wrinkle ridges were unable to analyze parameters such as area due to the lack of a basis for detailed characterization. Based on pixel-level details, the linear relationship between length and area was obtained, which not only explains the scientific value of pixel-level extraction results, but also provides a new basis for the study of the dynamics of lunar wrinkle ridges.

6. Conclusions

This study aimed to address the challenges associated with detecting lunar wrinkle ridges by developing a comprehensive data set tailored for deep learning applications and proposing a semantic segmentation model, DBR-Net. This model is specifically designed to leverage DEM data and aspect data for detecting lunar wrinkle ridges. The architecture of DBR-Net incorporates a dual-branch structure with a complementary feature fusion module that integrates an attention mechanism, allowing for enhanced flexibility feature extraction and efficient fusion of features from different data sources.

In DBR-Net, body features derived from the DEM representations are combined with edge features extracted from the aspect representations. This fusion enables a more precise capturing of the contours of lunar wrinkle ridges, effectively elevating the extraction results from a coarse ridge line representation to a finer pixel-level edge representation. To validate the efficacy of DBR-Net, it was compared with various mainstream deep learning semantic segmentation models through comparative experiments. These experiments not only confirmed the positive impact of aspect data on detection performance but also substantiated the effectiveness of the proposed method. DBR-Net outperforms typical semantic segmentation models in terms of precision (89.20%), recall (78.42%), F1-score (83.46%), and IoU (71.61%) on the lunar wrinkle ridges data set.

The proposed method was applied to lunar mare regions, resulting in the creation of a detailed distribution map of lunar mare wrinkle ridges. Based on pixel-level identification, we conducted a systematic parametric statistical analysis of the entire lunar mare wrinkle ridge segment, revealing a significant linear relationship between ridge length and area.

This finding provides a new basis for studying the dynamics of lunar wrinkle ridges. Additionally, the study identified six new potential lunar wrinkle ridges and their morphological characteristics were also analyzed and visualized. Overall, this study introduces DBR-Net as an effective model for lunar wrinkle ridge detection, significantly advancing the efficiency and accuracy of such detections in lunar terrain analysis.

ORCID iDs

Gaofeng Shu https://orcid.org/0000-0002-7098-7029

References

Barker, M. K., Mazarico, E., Neumann, G. A., et al. 2016, Icar, 273, 346
Burrough, P. A., McDonnell, R. A., & Lloyd, C. D. 2011, Principles of Geographical Information Systems (Oxford: Oxford Univ. Press)
Chen, L. C., Papandreou, G., Kokkinos, I., Murphy, K., & Yuille, A. L. 2017, ITPAM, 40, 834
Chen, L. C., Zhu, Y., Papandreou, G., Schroff, F., & Adam, H. 2018, Proc. of the European Conf. on Computer Vision (ECCV) (Berlin: Springer), 801
Ebel, P., Meraner, A., Schmitt, M., & Zhu, X.-X. 2020, ITGRS, 59, 5866
Feng, D., Haase-Schütz, C., Rosenbaum, L., et al. 2020, IEEE Transactions on Intelligent Transportation Systems, 22, 1341
Fergason, R., Hare, T., & Laura, J. 2018, HRSC and MOLA Blended Digital Elevation Model at 200m v2, Astrogeology PDS Annex, U.S. Geological Survey
He, K.-M., Zhang, X.-Y., Ren, S.-Q., & Sun, J. 2016, in Proc. IEEE Conf. Computer Vision and Pattern Recognition (CVPR) (Piscataway, NJ: IEEE), 770
Jiang, H.-K., Tian, X.-L., & Xu, A.-A. 2015, RAA, 15, 1604
Li, H., Li, R.-W., Shu, P., & Li, Y.-Q. 2024, RAA, 24, 045025
Lou, Y.-L., & Kang, Z.-Z. 2018, Science of Surveying and Mapping, 43, 155
Lu, T.-Q., Zhu, K., Chen, S.-B., et al. 2022, SciBu, 67, 1962
Micheal, A. A., Vani, K., & Sanjeevi, S. 2014, CG, 73, 122
Peng, Y., Bai, H.-C., Zhao, L.-M., et al. 2023, A&A, 677, A121
Qiao, L., Head, J. W., Wilson, L., Chen, J., & Ling, Z.-C. 2021, JGRE, 126, e2021JE006888
Schultz, R. A. 2000, JGRE, 105, 12035
Silburt, A., Ali-Dib, M., Zhu, C.-C., et al. 2019, Icar, 317, 27
Yao, M., & Chen, J. 2018, EM&P, 121, 45
Ye, Y.-X., Zhang, J.-C., Zhou, L., et al. 2024, ITGRS, 62, 1
Yue, Z., Li, W., Di, K., Liu, Z., & Liu, J. 2015, JGRE, 120, 978
Zhang, S., Liu, J.-Z., Michael, G., et al. 2024, RemS, 16, 1602